This is a preprint, the final version is subject to change, of the American Mineralogist (MSA)
Cite as Authors (Year) Title. American Mineralogist, in press.
DOI: https://doi.org/10.2138/am-2020-7470

Revision 3

Solubility of Na_2SO_4 in silica-saturated solutions: Implications for REE mineralization

HUAN CHEN, HAO CUI, RICHEN ZHONG*, YULING XIE*, CHANG YU, ZIMENG LI, YIFAN LING

School of Civil and Resource Engineering, University of Science and Technology Beijing, Beijing 100083, China

***Corresponding authors.** R. Zhong, Tel.: +8613671320438; E-mail: zhongrichen@126.com; Y. Xie, Tel.: +8613601236643; E-mail: yulingxie63@hotmail.com.

This is a preprint, the final version is subject to change, of the American Mineralogist (MSA)
Cite as Authors (Year) Title. American Mineralogist, in press.
DOI: https://doi.org/10.2138/am-2020-7470

ABSTRACT

Sulfate is traditionally considered to have retrograde solubility in aqueous solutions. However, our recent hydrothermal diamond anvil cell (HDAC) experiments have shown that the solubility of Na_2SO_4 changes from retrograde to prograde in the presence of silica, leading to the formation of sulfate-rich solutions at high temperatures, in line with observations on natural geofluids. In this study, we use synthetic inclusions of fused silica capillary capsules containing saturated Na_2SO_4 solutions and Na_2SO_4 crystals to quantitatively investigate the solubility of Na_2SO_4 at different temperatures in the Na_2SO_4-SiO_2-H_2O system. Sulfate concentrations were measured using Raman spectroscopy and calibrated using Cs_2SO_4 solutions with known concentrations. The solubility of crystalline Na_2SO_4 dropped slightly when heated from 50 to 225 °C and dramatically from 225 to 313 °C. At 313 °C, the Na_2SO_4 crystals began to melt, forming immiscible sulfate melt coexisting with the aqueous solution, with or without solid Na_2SO_4. With the formation of sulfate melt, the solubility of Na_2SO_4 was reversed to prograde (i.e., solubility increased considerably with increasing temperatures). The solubility of Na_2SO_4 in the measured solution was significantly higher than that predicted in the absence of SiO_2 over the entire temperature range (except for temperatures around 313 °C). This indicates that the presence of SiO_2 greatly changes the dissolution behavior of Na_2SO_4, which may be caused by the formation of a sulfate–silicate intermediates such as $Si(OH)_4SO_4^{2-}$. Considering that most crustal fluids are silica-saturated, the solubility curve of Na_2SO_4 obtained in this study can better reflect the characteristics of geofluids when compared to that of Na_2SO_4-H_2O binary system. At temperatures of 313–425 °C, the solubility of Na_2SO_4 increases with temperature

following the function $C_{sulfate} = -3173.7/T + 5.9301$, where $C_{sulfate}$ and T represents the solubility of Na_2SO_4 in mol/kg H_2O and temperature in Kelvin, respectively. As an application, this temperature-solubility relationship can be used to evaluate the sulfate contents in fluid inclusions that contain sulfate daughter minerals, based on the temperature of sulfate disappearance obtained from microthermometric analysis. The sulfate concentrations of the ore-forming fluids of the giant Maoniuping carbonatite-related rare earth element (REE) deposit (SW China) were calculated to be 4.67–4.81 *m* (mol/kg H_2O). These sulfate concentrations were then used as internal standards to calibrate the previously reported semi-quantitative results of laser ablation inductively coupled plasma mass spectrometry (LA-ICP-MS) analysis of REE-forming stage fluid inclusions at this deposit. The calculated Ce concentrations in the REE-mineralizing fluid range from 0.39 to 0.46 wt%. The high fluid REE contents suggest that the sulfate-rich fluids are ideal solvent for REE transport. A mass balance calculation was carried out to evaluate the minimal volume of carbonatite melt that was required for the formation the giant Maoniuping REE deposit. And the result indicates that the carbonatite dykes in the mining area are enough to provide the required fluids and metals, so a deep-seated magma chamber is not necessary for ore formation.

Keywords: Na_2SO_4 solubility, silica saturation, rare earth element, mineralizing fluid, FSCC

INTRODUCTION

Sulfate is the second most abundant solute in seawater and widely exists in the crustal mantle fluids and extraterrestrial aqueous environments, such as the surface of Mars and Europa (Chipera and Vaniman 2007; Mccord et al. 1998). Sulfate is abundant in some hydrothermal systems related to ore formation, such as volcanogenic massive sulfide (VMS) deposits (Yang et al. 2018) and copper porphyry deposits (Sun et al. 2013). Furthermore, syn-ore fluid inclusions containing sulfate daughter minerals have been reported in carbonatite-related rare earth element (REE) deposits, such as the world-class Bayan Obo in northern China (Xie et al. 2019) and the Maoniuping and Lizhuang in southwestern China (Xie et al. 2015). However, the presence of sulfate-rich geofluids contradict the knowledge that sulfate salts have retrograde solubility, which would lead to low concentrations of dissolved sulfate in high-temperature solutions (Seward et al. 2014).

Our recent study shows that the presence of dissolved silica is a key to changing the temperature dependence of sulfate solubility. In the presence of quartz and water (SiO_2-saturated fluid), Na_2SO_4 crystal will melt at ~300 °C, forming immiscible sulfate melt in coexistence with the aqueous phase. Once the melt forms, the solubility of Na_2SO_4 changes from retrograde to prograde, leading to the formation of sulfate-rich fluids at high temperatures (Cui et al. 2020). However, the solubility of Na_2SO_4 in the Na_2SO_4-SiO_2-H_2O system has not yet been quantified.

Sulfate-rich fluids are in close association with REE mineralization, and sulfate minerals are commonly observed in carbonatite-related REE deposits (Fan et al. 2016; Xie et al. 2015; Xu et al. 2015; Yu et al. 2014). In the current paradigm of REE mineralization, sulfate ion is

considered to be one of the potential ligands for REE migration (Migdisov et al. 2016). Moreover, previous LA-ICP-MS analyses on individual fluid inclusions at the Maoniuping and Lizhuang deposits showed strong REE signals in the sulfate-rich ore-fluids (Xie et al. 2015), manifesting the great ability of REE transport in sulfate-rich fluids. However, the REE contents in these inclusions were not quantified, due to the lack of available internal standards to calibrate the ICP-MS signals. The conventional approach to calibrate the trace element contents of inclusions is to use the concentration of dissolved NaCl as the internal standards, which can be obtained via the microthermometric analysis (Heinrich et al. 2003). However, this microthermometric method is not feasible for sulfate-predominated fluid systems, because the equation of states to calculate the concentrations of dissolved sulfate is lacking. Instead, the Ce/K ratio of the mineralization stage fluid inclusions hosted in fluorite was reported by Xie et al. (2015). If the temperature dependence of sulfate solubility is known, the sulfate contents in inclusions can be obtained via microthermometric methods, according to temperature of the disappearance of sulfate daughter minerals. The calculated sulfate concentrations can then be applied to calibrate the ICP-MS signals to obtain the REE concentrations in the fluids.

Experiments on mineral solubility are mostly conducted using hydrothermal autoclaves or piston-cylinder apparatus (Laudise et al. 1987; Tropper and Manning 2007), and the amounts of dissolved minerals can be analyzed using two major approaches. The first is to analyze the compositions of the separated (or quenched) solutions (e.g., Laudise et al. 1987) or weight losses of the reactants (e.g., Tropper and Manning 2007) after the devices are cooled down. If the solution is not quenchable, a design is required to separate solid reactants

from the solutions at high temperatures, to prevent re-precipitation during cooling (e.g., double capsule method) (Manning and Boettcher 1994). The second approach takes advantages of in situ spectroscopic analyses (mostly X-ray of synchrotron beam) to directly analyze concentrations of dissolved elements in the aqueous phase at high temperatures (e.g., Migdisov et al. 2009). However, neither of these methods can be applied to determine the solubility of Na_2SO_4 in silica-saturated solutions, due to the unusual high-temperature phase behaviors of the system. As revealed by our previous study (Cui et al. 2020), Na_2SO_4 crystals will melt at ~300 °C and thus the liquid sulfate cannot be physically separated from the aqueous solution. In addition, dissolved Na_2SO_4 will precipitate rapidly during cooling and the solution is thus unquenchable. Furthermore, due to the low X-ray energy of sulfur, its signal would be so weak that quantitative measurement of the sulfate concentration is not feasible using synchrotron technic. Raman spectra provide an ideal solution for the quantitative measurement sulfate ions (Schmidt and Seward 2017; Qiu et al. 2020), and fused silica capillary capsules (FSCCs) (Chou et al. 2008) are suitable for high-temperature in situ Raman observations, and can provide the silica-saturated condition.

In this study, fused silica capillary tubing was used to create synthetic fluid inclusions containing Na_2SO_4-supersaturated fluid system. The solubility of Na_2SO_4 was determined by in situ Raman spectroscopy at varying temperatures in the Na_2SO_4-SiO_2-H_2O system. Using the temperature-concentration relationship, we calculated the sulfate concentrations in the syn-ore fluorite-hosted fluid inclusions at the Maoniuping deposit and then use the concentrations to evaluate the REE contents in the fluid.

MATERIALS AND METHODS

Experimental designs for measuring the Na_2SO_4 solubility in a silica-saturated system

Sample preparation. FSCCs containing standard Cs_2SO_4 solutions and the Na_2SO_4-oversaturated system (solid Na_2SO_4 + saturated solution) were prepared using round cross-section fused silica capillary tubing with 100 μm of inner diameter and 365 μm of outer diameter (Polymicro Technologies, USA) (Wang et al. 2013). The polyimide coating of the tubing was burned off and the tubing was cleaned with ethyl alcohol (analytical grade reagent) before sample loading. The procedures of sealing the capillary tubes were described in detail by Chou et al. (2008) and Wang et al. (2013).

Cesium sulfate solutions were prepared from distilled deionized water and Cs_2SO_4 crystals (analytical grade reagent, 99.9% in purity; Shanghai Aladdin Bio-Chem Technology Co., Ltd.), and loaded into fused silica capillary tubing as standard samples. The concentrations of standard samples were set as 0.10, 0.49, 0.87, 1.91, and 2.90 *m* (molality, mol/kg H_2O), respectively. For the Na_2SO_4-bearing experimental samples, Na_2SO_4-saturated solutions and excess analytical grade Na_2SO_4 crystals (>99.0% in purity) were loaded into the fused silica capillary tubing successively. First, Na_2SO_4-saturated solution was loaded into the tubing as described in Wang et al. (2013). Then several Na_2SO_4 crystals were picked using a needle and loaded into the tubes. At last, the sealed capsules were centrifuged to ensure that all the solids are in one end of the capsule (Fig. 1a). This allowed the solution to remain saturated with respect to Na_2SO_4 as temperatures increases from 50 to 425 °C so that the measured sulfate concentrations can represent the solubility of Na_2SO_4.

The degree of filling (i.e., the volumetric ratio between the liquid phase and the entire

sample chamber) of standard samples were ~0.6. Two experimental samples were prepared with degrees of filling of 0.82 and 0.52. The former was heated from 50 to 425 °C, while the latter to only 313 °C to avoid explosion due to the high internal pressure. The prepared FSCCs were <1.5 cm in lengths so that could be placed to the sample chamber of the Linkam THMSG 600 heating–cooling stage. The sealed FSCCs were washed in an ultrasonic cleaner before Raman spectroscopic analyses.

Acquisition and processing of Raman spectra. Fused silica capillary capsules were placed on a Linkam THMSG 600 heating-cooling stage for temperature control with accuracy of ±0.1 °C, and the heating rate was set at 10 °C/min. To investigate the times that are required to achieve chemical equilibrium, three FSCCs containing solid Na_2SO_4 and saturated solution were maintained at 140 °C, 330 °C, and 400 °C, respectively. For each sample, Raman spectra of the solution were recorded repeatedly until the equilibrium of the system was acquired. Specifically, the times that are need for getting constant peak area ratios between the stretching vibration band of dissolved sulfate [$\nu_1(SO_4^{2-})$] and the OH stretching vibration band of water [($\nu_s H_2O$)] ($A_{sulfate}/A_{water}$) of the solutions were estimated (Fig. 2). It is revealed Na_2SO_4 saturation can be reached within 400 seconds, considering the uncertainties of the measurements (Fig. 2). Therefore, all the samples were held for 10 minutes at each temperature point before spectral acquisition. For standard samples, Raman spectra were collected at temperature interval of 50 °C for the temperature range of 50–450 °C. For experimental samples, the intervals were 50 °C and 25 °C for 50–200 °C and 200–450 °C, respectively. The Raman spectra for experimental samples were shown in Fig. 1b and those of standard samples in Appendix.

A Jobin Yvon/Horiba confocal LabRAM HR Evolution micro-Raman system at Peking University was used for Raman spectroscopic analyses. The ICS corrected Raman spectra were acquired with a 532-nm laser excitation (double frequency Nd: YAG), a 20× long-working distance objective with a 0.25 numerical aperture, and a 600-groove/mm grating. The laser power was 100 mW at the source. The confocal hole was set at 180 μm and the corresponding spectral pixel resolution was ~±2 cm^{-1}. The Raman spectral ranges of 800–1200 and 2500–4000 cm^{-1} were collected for the $v_1(SO_4^{2-})$ and $v_s(H_2O)$ bands, respectively, with an acquisition time of 20 s for each spectrum. The focus positions of the laser for all the samples, including experimental and standard, were set at the same depth by adjusting the focus distance till the boundaries of the cells are mostly clear (i.e., focus in the middle of the capillary). This can guarantee that the obtained Raman intensity are comparable among different samples (Schmidt 2017).

All Raman spectra measured in this study were processed using the PeakFit v. 4.11 software package (SYSAT Software Inc., USA) (Yuan et al. 2016). A linear baseline was subtracted after the spectral region of interest was selected. Then the spectra of $v_1(SO_4^{2-})$ and $v_s(H_2O)$ bands were fitted using a Gaussian + Lorentzian function and the peak areas of each band were obtained from the fitting results. For the $v_s(H_2O)$ band, the spectra were fitted with three sub-bands at ~3194 cm^{-1}, 3247 cm^{-1}, and 3444 cm^{-1}, respectively. The $v_1(SO_4^{2-})$ spectra were fitted as one component (Gaussian + Lorentzian function). The error of each fitted component was given by PeakFit. The total error of the peak area ratio, $A_{sulfate}/A_{water}$, was calculated based on the errors of each fitted component and the rules of error propagation (Taylor 1996).

Calibration of sulfate concentrations in experimental samples. The integrated $v_s(H_2O)$ intensity was used as the internal standards to normalize the peak area of $v_1(SO_4^{2-})$ band. In theory, the H_2O-normalized Raman peak area of SO_4^{2-} (i.e., $A_{sulfate}/A_{water}$) should exhibit a linear relationship with the sulfate concentration (Qiu et al. 2020). If the Raman parameters (e.g., laser wavelength, grating notch groove density, cumulative time, laser power, confocal hole size, objective working distance, etc.) remain constant, the relationship between sulfate concentration and H_2O-normalized Raman intensity at a given temperature can be retrieved by measuring the intensities of the $v_1(SO_4^{2-})$ and $v_s(H_2O)$ of standard samples with known sulfate concentrations. Then the sulfate concentrations in experimental samples can be obtained by plotting their $A_{sulfate}/A_{water}$ ratios on the calibration curve (*cf.*, Pokrovski and Dubessy 2015; Schmidt and Seward 2017).

Cesium sulfate solutions were chosen as the standard due to the high solubility of Cs_2SO_4 at room temperature, and thus standard samples with high sulfate concentrations can be prepared. Furthermore, Cs^+ is not prone to associate with SO_4^{2-} at elevated temperatures (i.e., negligible $CsSO_4^-$ and Cs_2SO_4(aq); inferred from the dissociation constant of KSO_4^- in Table 4 of Helgeson 1969), so the concentrations of free SO_4^{2-} are well defined (nearly equal to that of total sulfur). After each run of the heating-cooling circle, the Raman spectra of the standard and experimental samples were collected again at room temperature and compared with those collected at the beginning of the experiment. It is shown that the intensities of the $v_1(SO_4^{2-})$ and $v_s(H_2O)$ bands remained constant before and after heating, confirming the functional stability of the Raman spectrometer throughout the experiments and the reliability of the calibration results.

Pressure determination in FSCCs. Pressures inside the experimental samples were calculated using the ISOC program of the FLUIDS v.1 software package (Bakker 2003). Because the EoS (equation of state) of the Na_2SO_4-H_2O system is lacking, that of the NaCl-H_2O system (Zhang and Frantz 1987) was used as an approximation for pressure evaluation. The model NaCl-H_2O solutions were set to have the same molarities and homogenization temperature as those of the Na_2SO_4-H_2O solutions in the experimental samples. Errors in pressure estimation may be introduced by (i) using the EoS of NaCl-H_2O instead of Na_2SO_4-H_2O, and (ii) the thermal expansion of the cell at high temperatures (Chou et al. 2008). The latter might lead to the overestimation of the pressure at high temperatures, because the EoS-based pressure calculation requires the system to be isochoric (after vapor disappearance). We estimated that the calculated pressures are accurate within a factor 1–2.

Determination of experimental errors

The errors of the fitted peak areas for one component of $v_1(SO_4^{2-})$ band and three components of $v_s(H_2O)$ band were all directly obtained from PeakFit. According to the rules of error propagation (Taylor 1996), the total error of the peak area of $v_s(H_2O)$ band can be calculated by Eq. 1:

$$E_{W\ total} = E_{W1} + E_{W2} + E_{W3} \quad (1)$$

where E_{w1}, E_{w2}, and E_{w3} denote the errors of the three components of $v_s(H_2O)$ band, respectively, while $E_{w\ total}$ is the total error of the peak area of $v_s(H_2O)$. As for the area ratios between $v_1(SO_4^{2-})$ and $v_s(H_2O)$ bands, the propagated errors of the area ratios can be calculated by Eq. 2:

$$E_{Ratio} = (E_S/A_{sulfate} + E_{W\ total}/A_{water}) \times A_{normalized} \quad (2)$$

where $A_{normalized}$ is the peak area ratio between $v_1(SO_4^{2-})$ and $v_s(H_2O)$ bands; E_s is the error of the peak area of $v_1(SO_4^{2-})$; $A_{sulfate}$ and A_{water} are the areas of $v_1(SO_4^{2-})$ and $v_s(H_2O)$, respectively; and E_{Ratio} is the propagated error of the area ratios.

Validation of the measured solubility using hydrothermal diamond anvil cell

A hydrothermal diamond anvil cell (HDAC) (Bassett et al. 1996) was used to independently measure the solubility of Na_2SO_4 in the presence of quartz or amorphous silica, as a validation of the solubility-temperature relationship obtained using FSCCs. Doubly polished and gold-lined Re gaskets with a 400-μm diameter hole at the center were used to avoid the reaction between rhenium and sulfate ion at high temperatures (Pokrovski and Dubrovinsky 2011). In experimental run 1 (labeled as #HDAC_1), Na_2SO_4 solution (2.82 *m*; undersaturated at room temperature) was loaded in the sample chamber of the HDAC with a piece of silica glass. In experimental run 2 (labeled as #HDAC_2), Na_2SO_4 solution (2.50 *m*) was loaded with a gem-grade quartz piece from the Donghai deposit in China. The use of quartz instead of silica glass was to investigate the influence of crystalized/amorphous silica in changing the Na_2SO_4 solubility. When loading the Na_2SO_4 solutions into the sample chambers, the relative humidity in the room was controlled to be >60% to minimize the water loss due to evaporation, which may lead to an elevation in the Na_2SO_4 concentration (e.g., Schmidt 2009).

RESULTS

Construction of the relationship between $A_{sulfate}/A_{water}$ and $C_{sulfate}$

The spectra of the Cs_2SO_4 standard samples were processed to retrieve the relationships between the $A_{sulfate}/A_{water}$ ratios and the concentrations of sulfate ($C_{sulfate}$). These relationships vary with temperature, and thus were obtained at temperatures from 50 to 450 °C (Fig. 3). The relationships were retrieved as two steps. Firstly, by heating the five standard samples with different concentrations (0.10, 0.49, 0.87, 1.91, and 2.90 *m* for standard #1–5, respectively), the relationships between the measured $A_{sulfate}/A_{water}$ ratio and experimental temperature were obtained, yielding the temperature dependence of $A_{sulfate}/A_{water}$ for solutions with given concentrations (Fig. 3; Table 1). Secondly, for each temperature of interest, the $A_{sulfate}/A_{water}$-$C_{sulfate}$ relationships were determined by linear regression with five data points. Data points with low signal noise ratios were excluded (e.g. 200 and 250 °C for standard samples and 200 and 275 °C for experimental samples), and the missing points were obtained from the $A_{sulfate}/A_{water}$-T (temperature) relationship retrieved from the standard samples. In this way, the $A_{sulfate}/A_{water}$-$C_{sulfate}$ relationships were regressed for all temperature conditions with Pearson's correlation coefficients of $R^2 > 0.97$ (Fig. 4).

Measurement of the solubility of sulfate in the Na_2SO_4-SiO_2-H_2O system

Solubility of Na_2SO_4 in the SiO_2-saturated system. Based on the aforementioned $A_{sulfate}/A_{water}$-$C_{sulfate}$ relationships, the sulfate concentrations in the Na_2SO_4-saturated solutions within two FSCCs were calculated using the obtained $A_{sulfate}/A_{water}$ ratio (Fig. 5; Table 2). Because SO_4^{2-} was the only aqueous sulfur species that could be detected by the Raman spectra and the solution was saturated in Na_2SO_4, the determined SO_4^{2-} concentration can represent the solubility of Na_2SO_4. This result is consistent with Cui et al. (2020), where the pairing between Na^+ and SO_4^{2-} cannot be detected in the aqueous phase at high temperatures.

The estimated concentrations with increasing temperature were plotted in Fig. 5. For comparison, the solubility of Na_2SO_4 in pure water (silica-absent) was also calculated based on available thermodynamic properties using the HCh software package (Shvarov and Bastrakov 1999).

In both samples, Na_2SO_4 exhibited retrograde solubility at temperatures from 50 to 150 °C and 225 to 313 °C, and nearly constant solubility at 150–225 °C (Figs. 5 and 6a). The good reproducibility of the $C_{sulfate}$-T relationships obtained from the two samples indicates that the measurements were reliable. The Na_2SO_4 solubility in SiO_2-saturated solutions between 50 and 313 °C can be described by a cubic polynomial function with $R^2 = 0.970$ (Eq. 3; Fig. 6a):

$$C_{sulfate} = -5.4873 \times 10^{-7} \times T^3 + 7.1399 \times 10^{-4} \times T^2 - 3.0661 \times 10^{-1} \times T + 46.251 \quad (3)$$

where T is temperature in Kelvin.

As the temperature further increases, the solubility of Na_2SO_4 turned to be prograde (>313 °C; Fig. 5) due to the formation of sulfate melt (see below). The solubility of Na_2SO_4 reaches 3.88 *m* at 425 °C in the SiO_2-saturated system (Fig. 5; Table 2). For comparison, those in SiO_2-absent system remains retrograde through the whole temperature range and would decrease to ~0.6 *m* at 425 °C (Fig. 5). Even at temperatures below the melting temperature of Na_2SO_4 (~313 °C), the solubility of Na_2SO_4 in the SiO_2-saturated system is higher than that in the SiO_2-absent system (Fig. 5).

In the case of Na_2SO_4 dissolution at temperatures >313 °C, when the solubility is controlled by the dissolution of sulfate melt, the relationship between Na_2SO_4 solubility and

294 temperature was fitted as Eq. (4) with $R^2 = 0.993$ (Fig. 6b),

295 $$ln\ C_{sulfate} = -3173.7/T + 5.9301 \quad (4)$$

296 where T is temperature in Kelvin and $586.15 \leq T \leq 698.15$.

297 **Phase transitions of Na_2SO_4-SiO_2-H_2O system.** During the initial stage of heating,
298 Na_2SO_4 crystals began to precipitate around the pre-existing solid Na_2SO_4 in FSCCs with
299 increasing temperature. In particular, precipitation of large amounts of solid was observed at
300 temperatures >250 °C. This result is consistent with the measured solubility curve (Fig. 5), in
301 which the solubility of Na_2SO_4 gradually decreased from 3.16 (50 °C) to 2.67 *m* (250 °C) and
302 then sharply decreased to 1.25 *m* (313 °C). During heating, Na_2SO_4 crystals underwent two
303 solid-state phase transitions, from type V to III at 200–250 °C and from III to I at 250–300 °C,
304 which are consistent with previously reported experimental results (Cui et al. 2020). Cui et al.
305 (2020) demonstrated that the incipient melting of Na_2SO_4 is coupled with the phase transition
306 from type III to I, and this can be manifested by the solubility curve obtained in this study,
307 which shows a change from retrograde to prograde solubility at ~313 °C due to the formation
308 of sulfate melt (Fig. 5).

309 **Validation experiments using HDAC**

310 As temperature increased, the vapor in the HDAC gradually shrank and finally
311 homogenized into a liquid phase at 336 °C and 300 °C for the two runs of HDAC
312 experiments, respectively (Fig. 7). Upon heating, Na_2SO_4 crystals first precipitated from the
313 solution and then melted at higher temperatures. Finally, the sulfate melts re-dissolved into
314 the aqueous solution at 380 °C (sample #HDAC_1) and 351 °C (sample #HDAC_2). At these
315 temperatures, the Na_2SO_4 solubility would be estimated as 2.91 and 2.33 *m* based on Eq. 4 for

316 samples #HDAC_1 and 2, respectively. Comparing with the concentrations of the loaded
317 solutions (2.82 and 2.50 *m* for sample #HDAC_1 and 2), the differences are 3.37% and
318 −7.36%, respectively (Table 3).

319 The pressures at which solid Na_2SO_4 disappeared were estimated to be 56 MPa at
320 380 °C for sample #HDAC_1 and 66 MPa at 351 °C for sample #HDAC_2, which are much
321 lower than those in sample #FSCC_1 (238 MPa at 351 °C and 298 MPa at 380 °C). The
322 HDAC experiments indicated that the solubility-temperature relationship (Fig. 6b and Eq. 4)
323 can describe the solubility of Na_2SO_4 in SiO_2-saturated solutions with errors of <~8% within
324 the pressure range from 50 to at least 200 MPa (Table 4), regardless the form of solid SiO_2
325 (quartz crystal or amorphous silica). Therefore, this relationship can be applied to investigate
326 the Na_2SO_4 solubility in natural SiO_2-saturated crustal geofluids.

327

328 ## DISCUSSION

329 ### Influence of SiO_2 on the solubility of Na_2SO_4

330 Cui et al. (2020) reported that the presence of silica can significantly change the
331 dissolution behaviors of sulfate through the formation of sulfate melt. This accounts for the
332 rapid increase in the solubility of Na_2SO_4 at temperatures of >313 °C (Fig. 5). In this study,
333 we further observed that at lower temperatures, the presence of silica also elevates the
334 solubility of Na_2SO_4 (by ~35% at ~250 °C; Fig. 5) without the formation of sulfate melt (Fig.
335 5).

336 The changes in sulfate solubility may be a result of the formation of sulfate-silicic

complexes, such as $Si(OH)_4SO_4^{2-}$, in the presence of dissolved silica (Marshall and Chen 1982). Previous studies have shown that the formation of such complexes will increase the solubility of SiO_2 in sulfate-bearing solutions (Kotel'nikova and Kotel'nikov 2010; Wang et al. 2016). Here, we show that the elevation in solubility is mutual: the presence of silica could also enhance the dissolution of Na_2SO_4 and possibly other sulfate salts. Considering that quartz is ubiquitous in crustal rocks, the mobility of sulfate should be higher than previously estimated in crustal geofluids. Aside from the elevated solubility in the presence of silica, another factor that may lead to the formation of sulfate-rich fluids at high temperatures is the liquid-liquid immiscibility of sulfate solutions, which leads to the formation of a dense sulfate-rich liquid phase coexistent with the sulfate-poor solution (Wang et al. 2017; Wan et al. 2017).

Application to determine the fluid composition of ore-forming fluids of the carbonatite-related REE deposit

For fluid inclusions containing halite and other daughter minerals, salinities are measured based on the temperatures at which the daughter minerals completely dissolve into the aqueous phase (Potter and Clynne 1978). Salinity calculated using this approach is conventionally expressed as equivalent NaCl concentration because the presence of other electrolytes is inevitable but difficult to be known quantitatively. Similarly, the sulfate concentrations in inclusions that contain sulfate daughter minerals can be estimated using Eq. 4 and expressed as equivalent Na_2SO_4 contents, $C_{Na_2SO_4,\,eqv}$ (in m). This approach was applied to estimate the composition of the fluorite-hosted fluid inclusions from the Maoniuping deposit, the syn-ore mineral assemblage of which is characterized by the coexistence of

quartz and REE minerals (mainly bastnaesite) (Xie et al. 2015). Previous studies indicated that the syn-ore fluid inclusions contain large volumes of sulfate daughter minerals and they will first melt and finally disappear at 450–455 °C upon heating (Xie et al. 2015). Based on Eq. 4, these microthermometric results yielded sulfate concentrations ($C_{Na_2SO_4,\ eqv}$) ranging from 4.67 to 4.81 *m*.

Previous semi-quantitative LA-ICP-MS analyses of individual fluid inclusions (Xie et al. 2015) showed that the ore-fluids are mainly composed of dissolved Na-K-Sr-Ba-sulfates, with Na^+ and K^+ predominating over Sr^{2+} and Ba^{2+} (molar (K + Na)/(Sr + Ba) = 20), and Na^+ over K^+ (molar Na/K = 1.6). The ore-fluids were approximated as the Na-K-sulfate system in this calculations. The presence of K will lead to a deviation in the sulfate solubility from those calculated from simple Na_2SO_4 solution, but this deviation is not clear at present. We use the following equation to represent the influence of the presence of K:

$$C_{Na_2SO_4,\ eqv} = C_{Na_2SO_4,\ real} + A \times C_{K_2SO_4,\ real} \quad (5)$$

The form of Eq. 5 follows that of the well-studied NaCl-KCl-H_2O system (Allan et al. 2005), and $C_{Na_2SO_4,\ real}$ and $C_{K_2SO_4,\ real}$ are the real concentrations of Na_2SO_4 and K_2SO_4 in the fluids, respectively, and A is a factor describing the influence of the presence of K_2SO_4. For the NaCl-KCl-H_2O system, A is usually set as 0.5, indicating that KCl is more soluble than NaCl at the same temperature. However, the exact A value for the Na_2SO_4-K_2SO_4-SiO_2-H_2O system is unknown. Three hypothetical end-member values were used to calculate $C_{Na_2SO_4,\ real}$ from $C_{Na_2SO_4,\ eqv}$: (i) A = 0.4 representing that K_2SO_4 is more soluble than Na_2SO_4; (ii) A = 1 for equally soluble K_2SO_4 and Na_2SO_4, and (iii) A = 1.2 representing that Na_2SO_4 is more soluble. Tthe real sulfate concentration in the K_2SO_4-Na_2SO_4-H_2O system should be within

the three end member hypothesis. Given that the Na/K molar ratio is 1.6, these end member hypothesis yielded $C_{Na_2SO_4, real}$ ranging from 3.25 to 4.20 *m*. Based on microscopic observations, Xie et al. (2015) estimated that the inclusions contain 70–75 vol% of daughter minerals (mostly hydrated Na-K-Ca-sulfates). If the daughter minerals are all assumed to be mirabilite ($Na_2SO_4 \cdot 10H_2O$), this volume would yield a sulfate contents of 3.9 to 4.16 *m*, close to our estimation. Taking the 1000 × Ce/Na ratio (40.7) obtained from previous LA-ICP-MS results (Xie et al. 2015), the Ce concentrations in the ore-forming fluids were calculated to be 0.39–0.46 wt%.

Volume of carbonatite magma required for the formation of giant REE deposit

Geological and geochemical observations on the world-class Bayan Obo and the carbonatite-related REE deposits in southwestern China showed that sulfate-rich fluids were responsible for REE mineralization (Xie et al. 2009; 2015; 2019). Experimental studies also indicate that SO_4^{2-} forms strong bonds with REE^{3+} and is thus ideal ligand for hydrothermal REE transport (Migdisov et al. 2016; Cui et al. 2020). In this study, it is shown that 0.36–0.42 wt% of dissolved Ce can be transported by the natural sulfate-rich fluids. Given that Ce typically contributes half of the total REE resource (ΣREE) of carbonatite-related deposits (e.g., Fan et al. 2016), the ore-forming fluid at Maoniuping may have an ΣREE content as high as ~1 wt%, orders of magnitude higher than typical base metal-forming fluids (typically 10 to 1000 ppm of dissolved Cu, Pb, or Zn) (Yardley 2005).The high concentration of REEs in the ore-forming fluid implies that large volumes of hydrothermal fluid and carbonate melt may not be necessary for the formation of a giant REE deposit. In the case of the giant Maoniuping REE deposit with a reserve of 3.66×10^4 tons of Ce (He et al. 2018), 9.83×10^6

403 tons of ore-forming fluids were required to transport the metals, as calculated based on the
404 concentration of Ce in the fluid. Keppler (2003) showed that the water content in carbonatite
405 magma relates well to the pressure of the magma. Given the pressure of the magma intruding
406 at the Maoniuping (100–300 MPa) (Xie et al. 2009), the water content in the carbonatite melt
407 is estimated to be ~15 wt%. Taking the estimated density of the carbonatite rock of 2.78
408 g/cm^3 (*cf.*, the densities of calcite and dolomite) into account, 1.93×10^7–2.26×10^7 m^3 of
409 carbonatite is required to provide the metals and fluids for the Maoniuping deposit. It should
410 be noted that this volume is the lower limit required for the formation of the REE deposit.
411 First, not all the REEs were partitioned into the aqueous phase during the melt-fluid
412 separation. Second, not all REEs precipitated as ore minerals (e.g., bastnasite), with some
413 existing as solid solutions in refractory minerals (e.g., apatite). Finally, not all REE minerals
414 can be effectively concentrated to form economically signifcant REE orebodies, because
415 many of them were dispersed and precipitated as sub-economic host rocks with REE
416 anomalies.

417 Even though, the estimation of the magma volume required for ore formation provides
418 important constraints on the process of REE mineralization. Based on the geological map of
419 the mining area and orebody cross-sections (Xie et al. 2009), at least 1.44×10^8 m^3 of
420 carbonatite dykes were confirmed in the mine site of the Maoniuping deposit. This volume is
421 nearly six times larger than the minimal magma volume required for REE mineralization.
422 This indicates that the known carbonatite dykes are sufficient to account for the formation of
423 the giant REE deposit and s deep-seated magma chamber is not necessary, consistent with the
424 conclusion by Xie et al. (2015).

IMPLICATIONS

This study together with our previous research (Cui et al. 2020) show that the dissolution and melting process of sodium sulfate can be significantly influenced by the presence of trace amount of silica, which is traditionally regarded as an inert component in fluid system. Taken the ubiquitous presence of silica in the earth's crust, this finding implies that our current understandings on the high-temperature hydrothermal behaviors of sulfates, and possibly other types of minerals, may need to be reevaluated, as dissolved silica can be active in reacting with other ligands. Furthermore, this study implies that the influences of dissolved silica cannot be neglected and should be envisaged for hydrothermal experiments using technics such as FSCC and synthetic fluid inclusion in quartz (e.g., Kotel'nikova and Kotel'nikov 2010).

ACKNOWLEDGEMENTS

We would like to thank Ying Cui and the School of Earth and Space Sciences of Peking University for assistance in conducting Raman spectrum analysis. We would also like to thank two anonymous reviewers for their suggestions in improving the manuscript. This work was supported by the National Natural Science Foundation of China (grant nos. 41472072, 41872078, and 41502069), the State Key Research Plan (grant no. 2017YFC0601302), the Australian Research Council (grant no. DP190100216), the Young Elite Scientists Sponsorship Program by CAST (grant no. YESS), and the Fundamental Research Funds for the Central Universities (grant no. FRF-TP-18-017A3).

REFERENCES CITED

Allan, M.M., Yardley, B.W.D., Forbes, L.J., Shmulovich, K.I., Banks, D.A., and Shepherd, T.J. (2005) Validation of LA-ICP-MS fluid inclusion analysis with synthetic fluid inclusions. American Mineralogist, 90, 1767−1775.

Bakker, R.J. (2003) Package *FLUIDS* 1. Computer programs for analysis of fluid inclusion data and for modelling bulk fluid properties. Chemical Geology, 194, 3−23.

Bassett, W.A., Wu, T.C., Chou, I-M., Haselton, H.T. Jr., Frantz, J., Mysen, B.O., Huang, W.L., Sharma, S.K., and Schiferl, D. (1996) The hydrothermal diamond anvil cell (HDAC) and its applications: special publication. Geochemical Society, 5, 261–272.

Chipera, S.J., and Vaniman, D.T. (2007) Experimental stability of magnesium sulfate hydrates that may be present on Mars. Geochimica et Cosmochimica Acta, 71, 241−250.

Chou, I-M., Song, Y., and Burruss, R.C. (2008) A new method for synthesizing fluid inclusions in fused silica capillaries containing organic and inorganic material. Geochimica et Cosmochimica Acta, 72, 5217−5231.

Cui, H., Zhong, R.C., Xie, Y.L., Yuan, X.Y., Liu, W.H., Brugger, J., and Yu, C. (2020) Forming sulfate- and REE-rich fluids in the presence of quartz. Geology, 48, 145−148.

Fan, H.R., Yang, K.F., Hu, F.F., Liu, S., and Wang, K.Y. (2016) The giant Bayan Obo REE-Nb-Fe deposit, China: Controversy and ore genesis. Geoscience Frontiers, 7, 335−344.

He, Y., Deng, T., Hao, X.F., Wen, H., and Xu, T. (2018) Indication of bastnasite heavy

minerals of Mianxi REE Belt. Journal of the Chinese Rare Earth Society, 64, 299−345 (in Chinese).

Heinrich, C.A., Pettke, T., Halter, W.E., Aigner-Torres, M., Audétat, A., Günther, D., Hattendorf, B., Bleiner, D., Guillong, M., and Horn, I. (2003) Quantitative multi-element analysis of minerals, fluid and melt inclusions by laser-ablation inductively-coupled-plasma mass-spectrometry. Geochimica et Cosmochimica Acta, 67, 3473–3496.

Helgeson, H.C. (1969) Thermodynamics of hydrothermal systems at elevated temperatures and pressures. American Journal of Science, 267, 729–804.

Keppler, H. (2003) Water solubility in carbonatite melts. American Mineralogist, 88, 1822−1824.

Kotel'nikova, Z.A., and Kotel'nikov, A.R. (2010) Immiscibility in sulfate-bearing fluid systems at high temperatures and pressures. Geochemistry International, 48, 381−389.

Laudise, R.A., Schneemeyer, L.F., and Barns, R.L. (1987) Crystal growth of high temperature superconductors—Problems, successes, opportunities. Journal of Crystal Growth, 85, 569−575.

Manning, C.E., and Boettcher, S.L. (1994) Rapid-quench hydrothermal experiments at mantle pressures and temperatures. American Mineralogist, 79, 1153−1158.

Marshall, W.L., and Chen, C.T.A. (1982) Amorphous silica solubilities V. Predictions of solubility behavior in aqueous mixed electrolyte solutions to 300 °C. Geochimica et Cosmochimica Acta, 46, 289−291.

McCord, T.B., Hansen, G.B., Fanale, F.P., Carlson, R.W., Matson, D.L., Johnson, T.V., Smythe, W.D., Crowley, J.K., Martin, P.D., Ocampo, A., and others. (1998) Salts on Europa's surface detected by Galileo's near infrared mapping spectrometer. Science, 280, 1242−1245.

Migdisov, A., Williams-Jones, A.E., Brugger, J., and Caporuscio, F.A. (2016) Hydrothermal transport, deposition, and fractionation of the REE: Experimental data and thermodynamic calculations. Chemical Geology, 439, 13−42.

Pokrovski, G.S., and Dubessy, J. (2015) Stability and abundance of the trisulfur radical ion S_3^- in hydrothermal fluids. Earth and Planetary Science Letters, 411, 298−309.

Pokrovski, G.S., and Dubrovinsky, L.S. (2011) The S_3^- ion is stable in geological fluids at elevated temperatures and pressures. Science, 331, 1052−1054.

Potter, R.W. II, and Clynne, M.A. (1978) Solubility of highly soluble salts in aqueous media. Part 1, NaCl, KCl, $CaCl_2$, Na_2SO_4, and K_2SO_4 solubilities to 100 °C. Journal of Research of The US Geological Survey, 6, 701–705.

Qiu, Y., Yang, Y.X., Wang, X.L., Wan, Y., Hu, W.X., Lu, J.J., Tao, G.L., Li, Z., and Meng, F.W. (2020) In situ Raman spectroscopic quantification of aqueous sulfate: Experimental calibration and application to natural fluid inclusions. Chemical Geology, 533. https://doi.org/10.1016/j.chemgeo.2019.119447.

Schmidt, C. (2009) Raman spectroscopic study of a H_2O + Na_2SO_4 solution at 21–600 °C and 0.1 MPa to 1.1 GPa: Relative differential ν_1-SO_4^{2-} Raman scattering cross sections and evidence of the liquid-liquid transition. Geochimica et Cosmochimica Acta, 73, 425−437.

510 Schmidt, C., and Seward, T.M. (2017) Raman spectroscopic quantification of sulfur species
511 in aqueous fluids: Ratios of relative molar scattering factors of Raman bands of H_2S, HS^-,
512 SO_2, HSO_4^-, SO_4^{2-}, $S_2O_3^{2-}$, S_3^- and H_2O at ambient conditions and information on
513 changes with pressure and temperature. Chemical Geology, 467, 64–75.

514 Seward, T.M., Williams-Jones, A.E., and Migdisov, A.A. (2014) The chemistry of metal
515 transport and deposition by ore-forming hydrothermal fluids. In K.K. Turekian, and H.D.
516 Holland, Eds., Treatise on Geochemistry, p. 29–57. Elsevier, Amsterdam, Netherlands.

517 Shvarov, Y.V., and Bastrakov, E.N. (1999) HCh: a software package for geochemical
518 equilibrium modelling. User's guide (Australian Geological Survey Organization,
519 Canberra, 1999), Record 199/25.

520 Sun, W.D., Liang, H.Y., Ling, M.X., Zhan, M.Z., Ding, X., Zhang, H., Yang, X.Y., Li, Y.L.,
521 Ireland, T.R., Wei, Q.R., and others. (2013) The link between reduced porphyry copper
522 deposits and oxidized magmas. Geochimica et Cosmochimica Acta, 103, 263−275.

523 Taylor, J.R. (1996) An Introduction to Error Analysis. University Science Books, Sausalito.

524 Tropper, P., and Manning, C.E. (2007) The solubility of fluorite in H_2O and H_2O-NaCl at
525 high pressure and temperature. Chemical Geology, 242, 299−306.

526 Wan, Y., Wang, X.L., Hu, W.X., Chou, I-M., Wang, X.Y., Chen, Y., and Xu, Z.M. (2017) In
527 situ optical and Raman spectroscopic observations of the effects of pressure and fluid
528 composition on liquid-liquid phase separation in aqueous cadmium sulfate solutions
529 (≤400 °C, 50MPa) with geological and geochemical implications. Geochimica et
530 Cosmochimica Acta, 211, 133−152.

Wang, X.L., Chou, I-M., Hu, W.X., and Burruss, R.C. (2013) *In situ* observations of liquid-liquid phase separation in aqueous $MgSO_4$ solutions: Geological and geochemical implications. Geochimica et Cosmochimica Acta, 103, 1−10.

Wang, X.L., Wan, Y., Hu, W.X., Chou, I-M., Cao, J., Wang, X.Y., Wang, M., and Li, Z. (2016) *In situ* observations of liquid-liquid phase separation in aqueous $ZnSO_4$ solutions at temperatures up to 400 °C: Implications for Zn^{2+}-SO_4^{2-} association and evolution of submarine hydrothermal fluids. Geochimica et Cosmochimica Acta, 181, 126−143.

Wang, X.L., Wang, X.Y., Chou, I-M., Hu, W.X., Wan, Y., and Li, Z. (2017) Properties of lithium under hydrothermal conditions revealed by in situ Raman spectroscopic characterization of Li_2O-SO_3-H_2O (D_2O) systems at temperatures up to 420 °C. Chemical Geology, 451, 104−115.

Xie, Y.L., Hou, Z.Q., Yin, S.P., Dominy, S.C., Xu, J.H., Tian, S.H., and Xu, W.Y. (2009) Continuous carbonatitic melt–fluid evolution of a REE mineralization system: Evidence from inclusions in the Maoniuping REE deposit, Western Sichuan, China. Ore Geology Reviews, 36, 90−105.

Xie, Y.L., Li, Y.X., Hou, Z.Q., Cooke, D.R., Danyushevsky, L., Dominy, S.C., and Yin, S.P. (2015) A model for carbonatite hosted REE mineralization—the Mianning−Dechang REE belt, Western Sichuan Province, China. Ore Geology Reviews, 70, 595−612.

Xie, Y.L., Qu, Y.W., Yang, Z.F., Liang, P., Zhong, R.C., Wang, Q.W., Xia, J.M., and Li, B.C. (2019) Giant Bayan Obo Fe-Nb-REE deposit: Progresses, controversaries and new understandings. Mineral Deposits, 38, 983−1003 (in Chinese).

552 Xu, C., Kynicky, J., Chakhmouradian, A.R., Li, X.H., and Song, W.L. (2015) A case example
553 of the importance of multi-analytical approach in deciphering carbonatite petrogenesis in
554 South Qinling orogen: Miaoya rare-metal deposit, central China. Lithos, 227, 107−121.

555 Yang, C.D., Chai, F.M., Yang, F.Q., Santosh, M., Xu, Q.F., and Wang, W. (2018) Genesis of
556 the Huangtupo Cu-Zn deposit, Eastern Tianshan, NW China: Constraints from geology,
557 Rb-Sr and Re-Os geochronology, fluid inclusions, and H-O-S-Pb isotopes. Ore Geology
558 Reviews, 101, 725−739.

559 Yardley, B.W.D. (2005) Metal concentrations in crustal fluids and their relationship to ore
560 formation. Economic Geology, 100, 613−632.

561 Yu, X.F., Tang, H.S., and Li, D.P. (2014) Study on the mineralization of Chishan rare earth
562 element deposit related to alkaline rock, Shandong Province. Acta Geologica Sinica
563 (English Edition), 88, 480−481.

564 Yuan, X.Y., Mayanovic, R.A., and Zheng, H.F. (2016) Determination of pressure from
565 measured Raman frequency shifts of anhydrite and its application in fluid inclusions and
566 HDAC experiments. Geochimica et Cosmochimica Acta, 194, 253−265.

567 Zhang, Y.G., and Frantz, J.D. (1987) Determination of the homogenization temperatures and
568 densities of supercritical fluids in the system NaCl-KCl-$CaCl_2$-H_2O using synthetic fluid
569 inclusions. Chemical Geology, 64, 335–350.

570 **Figure Caption**

571 **Fig. 1.** (**a**) Schematic diagram of the experimental method in FSCC experiments. (**b**) The
572 microscopic photo of the experimental sample at 100 and 350 ℃ along with Raman spectra
573 of the saturated solution at varying temperatures. Abbreviations: Aq = aqueous solution, S =
574 solid Na_2SO_4, V = vapor phase, M = sulfate melt.

575 **Fig. 2.** The investigation of equilibrium time of experimental samples. The $A_{sulfate}/A_{water}$ in the
576 experimental samples varied with experimental duration. The data suggested that equilibrium
577 was attained after ~400 s at 140 ℃ and 330 ℃ and after ~300 s at 400 ℃. Whiskers
578 represented 95% confidence intervals.

579 **Fig. 3.** Changes in peak area ratios $A_{sulfate}/A_{water}$ of standard samples with increasing
580 temperature (T). The standard samples (standard #1–5) have different concentrations (0.10,
581 0.49, 0.87, 1.91, and 2.90 m) of Cs_2SO_4. The relationships between the measured $A_{sulfate}/A_{water}$
582 and temperatures were regressed.

583 **Fig. 4.** The relationships between the concentrations of Cs_2SO_4 ($C_{sulfate}$) and peak area ratios
584 $A_{sulfate}/A_{water}$ at each temperature. These relationships were used to calibrate the concentrations
585 of sulfate in the experimental samples.

586 **Fig. 5.** The solubility of Na_2SO_4 in silica-saturated solutions at temperatures of 50–425 °C. In
587 addition, the solubility curve of Na_2SO_4 in SiO_2-free solutions is also shown for comparison
588 (calculated using the HCh program, Shvarov and Bastrakov 1999). Whiskers represented 95%
589 confidence intervals.

590 **Fig. 6.** The temperature dependence of the Na_2SO_4 solubility in SiO_2-saturated solutions. (**a**)
591 The Na_2SO_4 solubility within the temperature range of 50–313 °C. (**b**) The Na_2SO_4 solubility

592 under high temperatures (>313 °C).

593 **Fig. 7.** Phase behaviors of Na_2SO_4-SiO_2-H_2O system in an HDAC experiment (sample
594 #HDAC_2) at 180 °C, 300 °C, and 351 °C. Abbreviations: Aq = aqueous solution, S = solid
595 Na_2SO_4, V = vapor phase, Qtz = quartz, V= vapor phase.

596

Tables

TABLE 1. The relationships between $A_{sulfate}/A_{water}$ and temperature (T) at different Cs_2SO_4 concentrations. $A_{sulfate}/A_{water}$ is the peak area ratio between $v_1(SO_4^{2-})$ and $v_s(H_2O)$ bands and T is the temperature in ℃.

Sample no.	Concentration (m)	Equation and R^2
standard #1	0.10	$A_{sulfate}/A_{water} = 2 \times 10^{-5}T + 2.7 \times 10^{-3}$, $R^2 = 0.548$
standard #2	0.49	$A_{sulfate}/A_{water} = 4.42 \times 10^{-5}T + 1.72 \times 10^{-2}$, $R^2 = 0.938$
standard #3	0.87	$A_{sulfate}/A_{water} = 2.62 \times 10^{-7}T^2 - 2.92 \times 10^{-5}T + 3.72 \times 10^{-2}$, $R^2 = 0.981$
standard #4	1.91	$A_{sulfate}/A_{water} = 6.76 \times 10^{-9}T^3 - 3.77 \times 10^{-6}T^2 + 7.01 \times 10^{-4}T + 5.26 \times 10^{-2}$, $R^2 = 0.987$
standard #5	2.90	$A_{sulfate}/A_{water} = 8.50 \times 10^{-9}T^3 - 5.02 \times 10^{-6}T^2 + 1.01 \times 10^{-3}T + 7.81 \times 10^{-2}$, $R^2 = 0.978$

This is a preprint, the final version is subject to change, of the American Mineralogist (MSA)
Cite as Authors (Year) Title. American Mineralogist, in press.
DOI: https://doi.org/10.2138/am-2020-7470

612 TABLE 2. The measured sulfate solubility in SiO_2-saturated Na_2SO_4 solutions (Sample
613 #FSCC_1–2) at temperatures from 50 to 425 °C.

T (°C)	$A_{sulfate}/A_{water}$	Error for $A_{sulfate}/A_{water}$	$C_{sulfate}$ (m)	Error for $C_{sulfate}$ ($\pm m$)	Sample
50	0.13	0.02	3.10	0.35	#FSCC_1
100	0.13	0.01	2.92	0.26	#FSCC_1
150	0.13	0.02	2.78	0.48	#FSCC_1
225	0.15	0.01	2.91	0.42	#FSCC_1
275	0.13	0.01	2.60	0.11	#FSCC_1
300	0.11	0.01	1.65	0.18	#FSCC_1
325	0.11	0.02	1.82	0.36	#FSCC_1
350	0.14	0.00	2.34	0.05	#FSCC_1
375	0.20	0.00	2.89	0.07	#FSCC_1
400	0.26	0.01	3.41	0.07	#FSCC_1
425	0.35	0.01	3.88	0.09	#FSCC_1
50	0.14	0.02	3.22	0.37	#FSCC_2
100	0.13	0.01	2.84	0.20	#FSCC_2
150	0.13	0.01	2.70	0.20	#FSCC_2
250	0.15	0.00	2.71	0.09	#FSCC_2
275	0.14	0.01	2.42	0.18	#FSCC_2
300	0.10	0.01	1.84	0.16	#FSCC_2
313	0.07	0.01	1.25	0.11	#FSCC_2

614

615

616 ABLE 3. The solubility of Na_2SO_4 in SiO_2-saturated solutions, results of HDAC experiments.

Sample	Silica species	Actual concentration (m)	Calculated concentration (m)	$T_{h,\,tot}$ [a] (°C)	P [b] (MPa)
#HDAC_1	glassy silica	2.82	2.91	380	56
#HDAC_2	quartz crystal	2.50	2.33	351	66

617 [a] $T_{h,\,tot}$ = totally homogenization temperature.

618 [b] P = pressure at $T_{h,\,tot}$.

This is a preprint, the final version is subject to change, of the American Mineralogist (MSA)
Cite as Authors (Year) Title. American Mineralogist, in press.
DOI: https://doi.org/10.2138/am-2020-7470

619

620 TABLE 4. Pressure estimation for FSCCs with different degrees of filling.

Sample	Degree of filling	$T_{h,\ vapor}$ (°C) [a]	P_{425} (MPa) [b]
#FSCC_1	0.82	320	139
#FSCC_2	0.52	371	73

621 [a] $T_{h,\ vapor}$ = aqueous-vapor homogenization temperature within the FSCC.

622 [b] P_{425} = the calculated inner pressure of FSCC at 425 °C.

Fig. 1

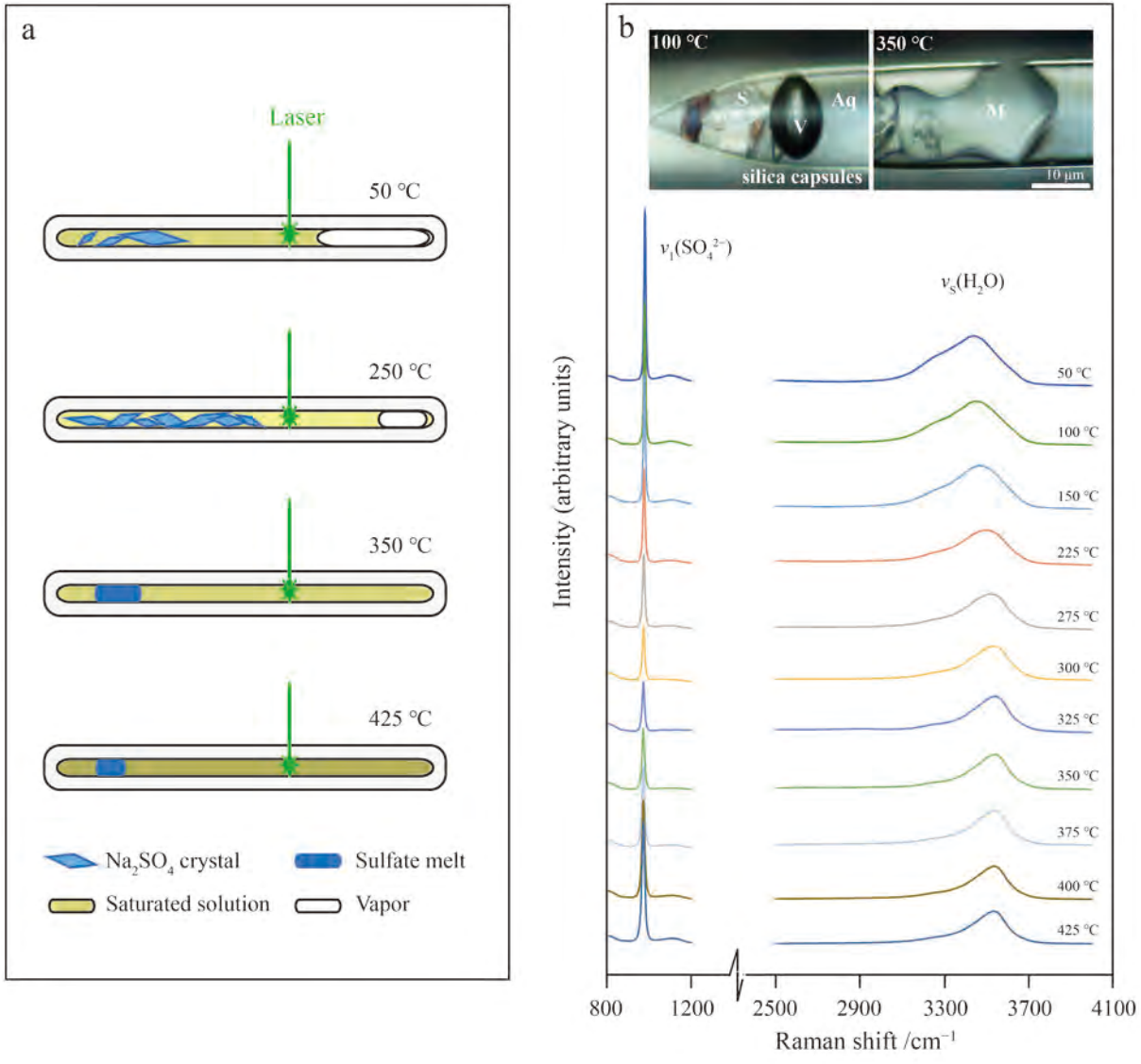
a
Laser
50 °C
250 °C
350 °C
425 °C
Na2SO4 crystal
Sulfate melt
Saturated solution
Vapor
b
100 °C
350 °C
S
Aq
V
M
silica capsules
10 μm
ν1(SO4 2−)
νS(H2O)
Intensity (arbitrary units)
50 °C
100 °C
150 °C
225 °C
275 °C
300 °C
325 °C
350 °C
375 °C
400 °C
425 °C
800
1200
2500
2900
3300
3700
4100
Raman shift /cm−1

Fig. 2

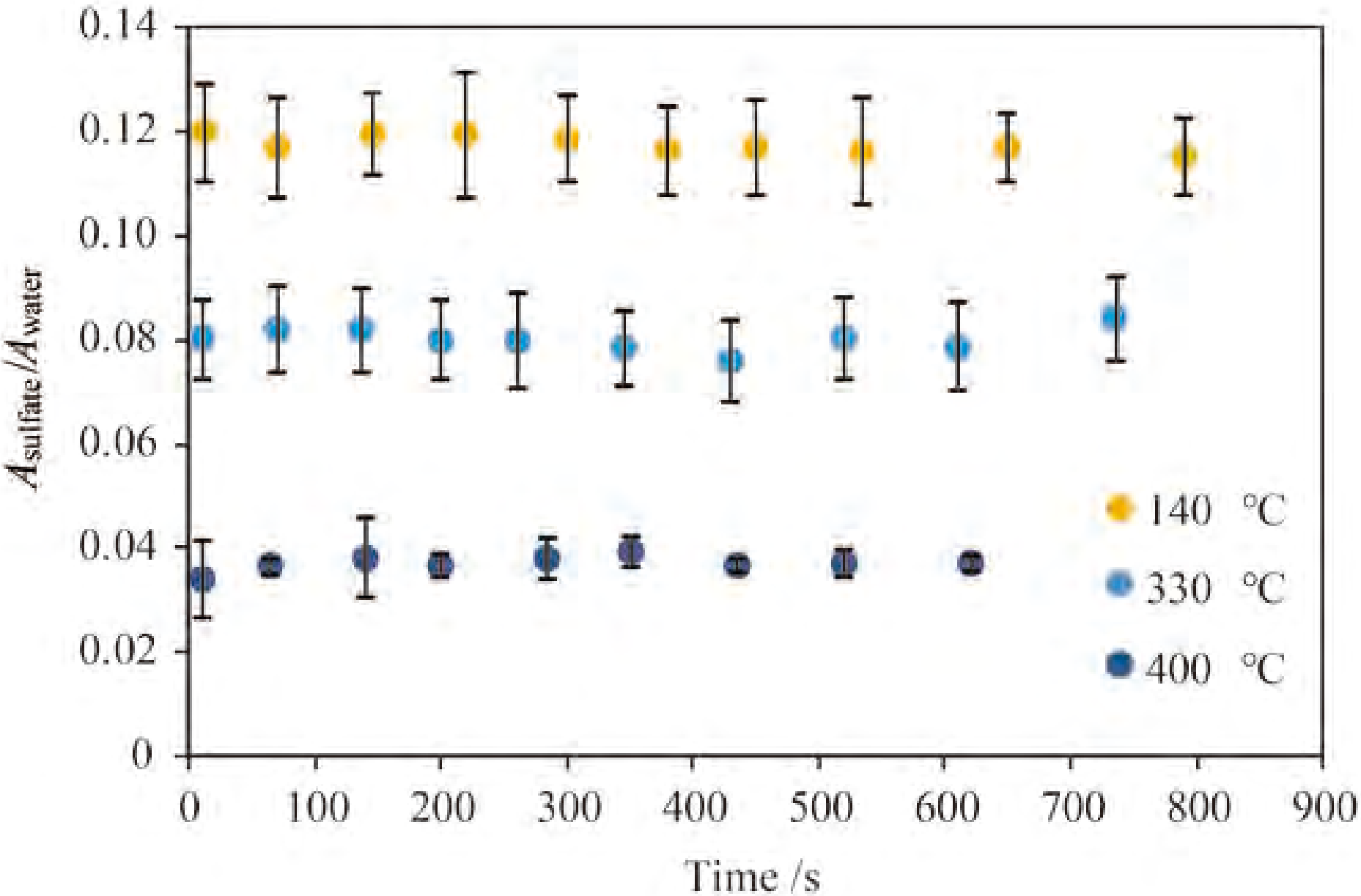
0.14
0.12
0.10
0.08
0.06
0.04
0.02
0
$A_{sulfate}/A_{water}$
0
100
200
300
400
500
600
700
800
900
Time /s
140 °C
330 °C
400 °C

Fig. 3

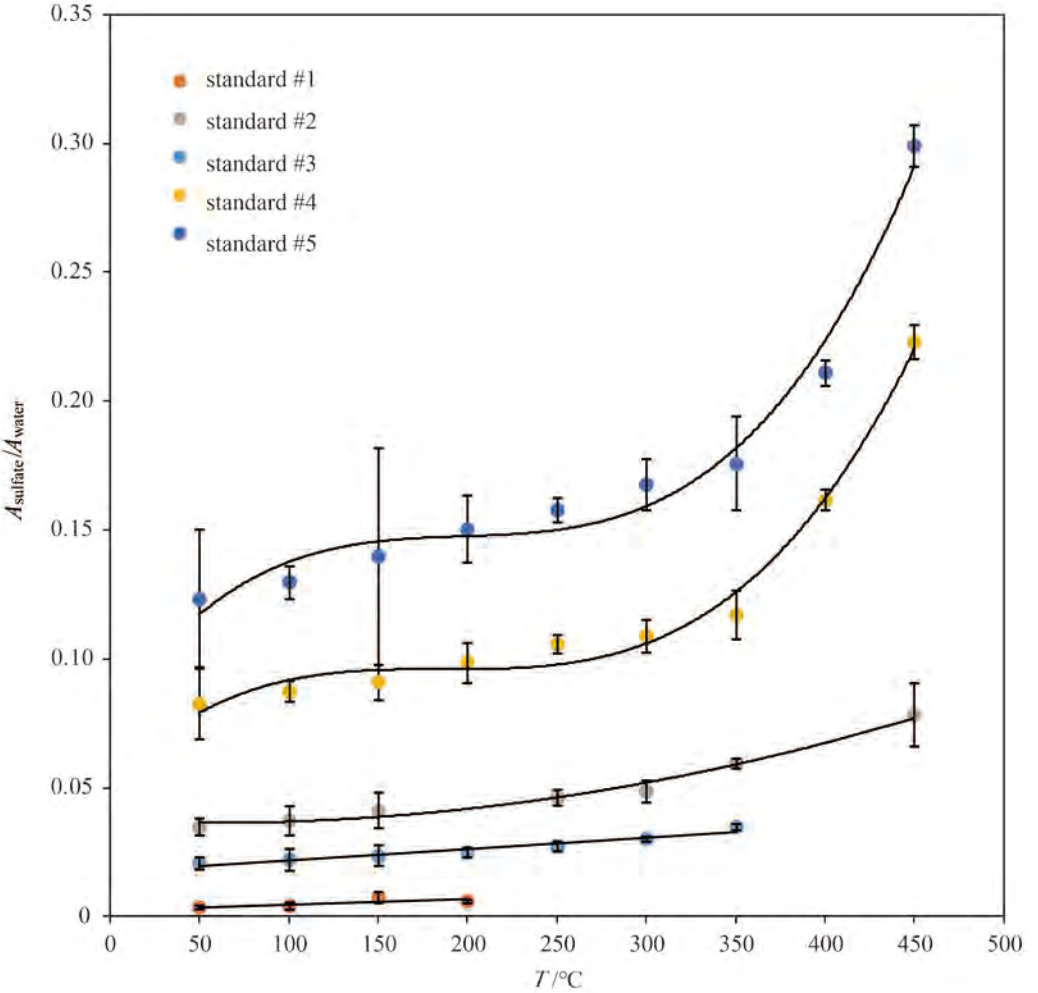
standard #1
standard #2
standard #3
standard #4
standard #5
$A_{sulfate}/A_{water}$
T /°C
0.35
0.30
0.25
0.20
0.15
0.10
0.05
0
0
50
100
150
200
250
300
350
400
450
500

Fig. 4

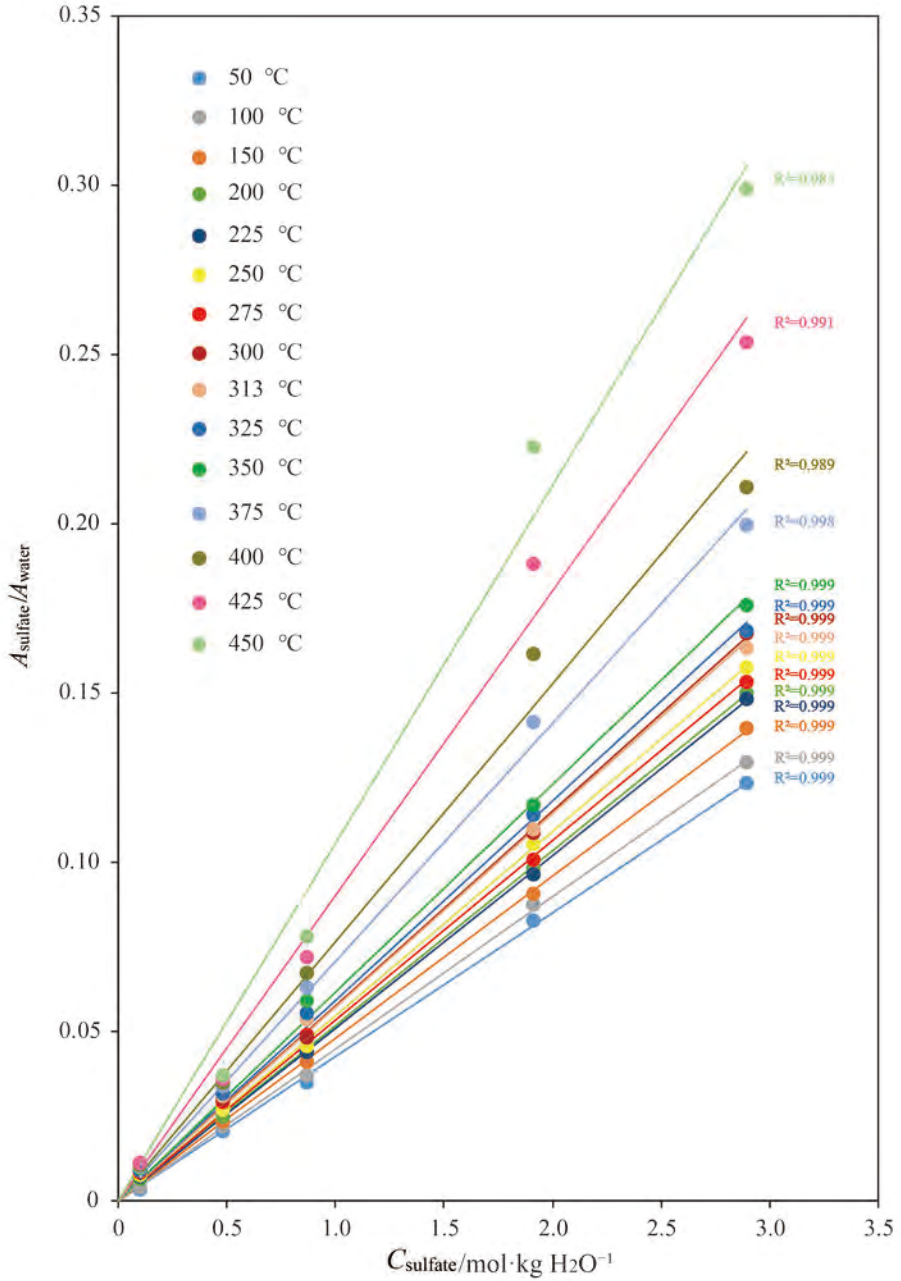
50 °C
100 °C
150 °C
200 °C
225 °C
250 °C
275 °C
300 °C
313 °C
325 °C
350 °C
375 °C
400 °C
425 °C
450 °C
R²=0.981
R²=0.991
R²=0.989
R²=0.998
R²=0.999
R²=0.999
R²=0.999
R²=0.999
R²=0.999
R²=0.999
R²=0.999
R²=0.999
R²=0.999
R²=0.999
R²=0.999
0.35
0.30
0.25
0.20
0.15
0.10
0.05
0
0
0.5
1.0
1.5
2.0
2.5
3.0
3.5
$A_{sulfate}/A_{water}$
$C_{sulfate}$/mol·kg H_2O^{-1}

Fig. 5

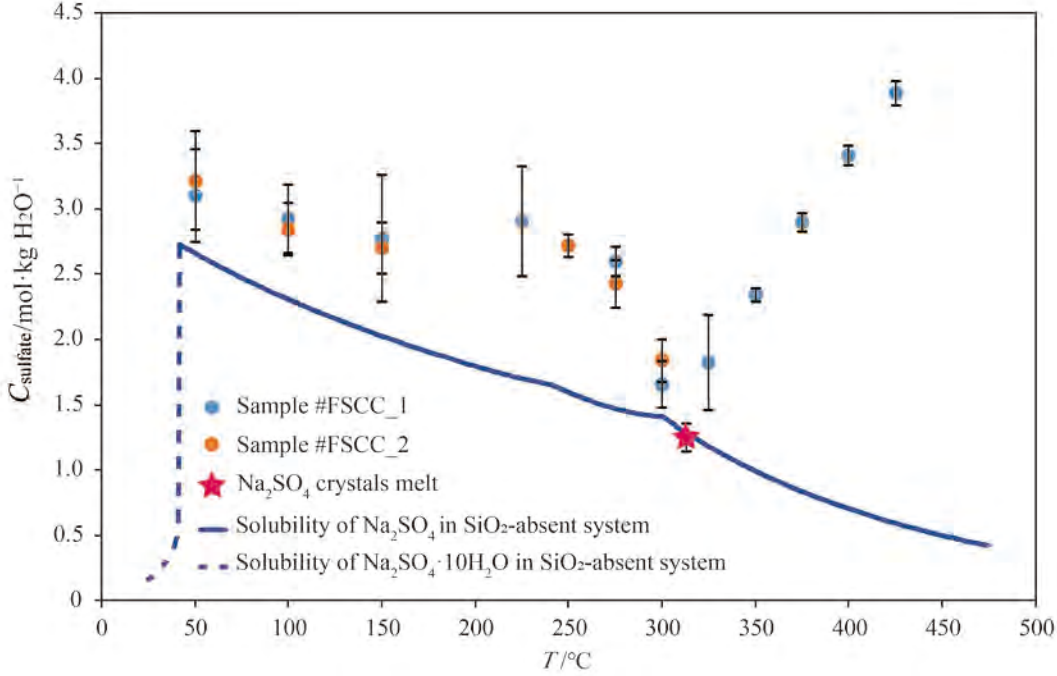
4.5
4.0
3.5
3.0
2.5
2.0
1.5
1.0
0.5
0
$C_{sulfate}$/mol·kg H_2O^{-1}
0
50
100
150
200
250
300
350
400
450
500
T/°C
Sample #FSCC_1
Sample #FSCC_2
Na_2SO_4 crystals melt
Solubility of Na_2SO_4 in SiO_2-absent system
Solubility of $Na_2SO_4 \cdot 10H_2O$ in SiO_2-absent system

Fig. 6

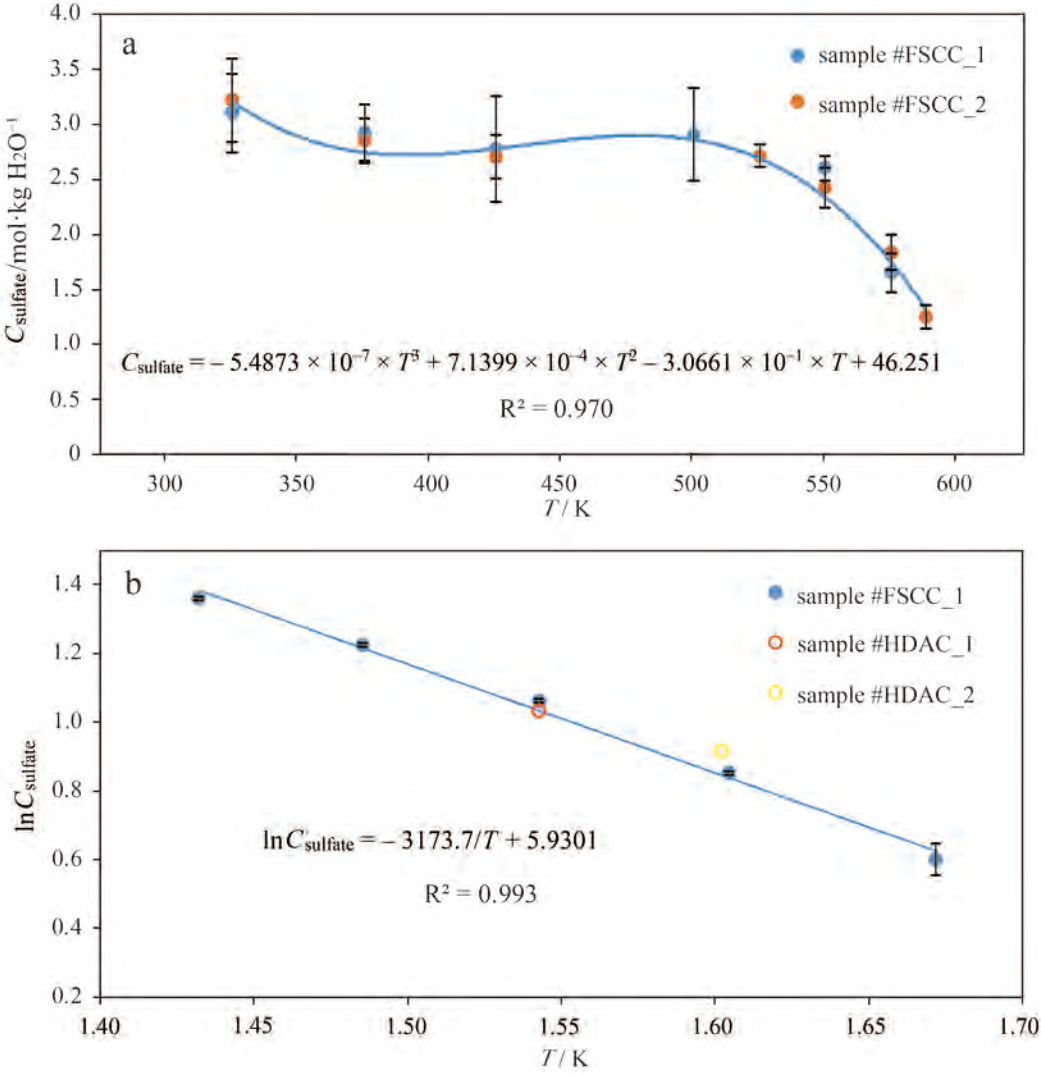
a
sample #FSCC_1
sample #FSCC_2
$C_{sulfate}$/mol·kg H_2O^{-1}
$C_{sulfate} = -5.4873 \times 10^{-7} \times T^3 + 7.1399 \times 10^{-4} \times T^2 - 3.0661 \times 10^{-1} \times T + 46.251$
$R^2 = 0.970$
T / K
b
sample #FSCC_1
sample #HDAC_1
sample #HDAC_2
$\ln C_{sulfate}$
$\ln C_{sulfate} = -3173.7/T + 5.9301$
$R^2 = 0.993$
T / K

Fig. 7